(Received 17 April 2025, Accepted 3 June 2025, Scheduled 21 June 2025)

Hybrid Multi-Scale Simulation Workflow for Installation and Isolation of Flush-Mounted Antennas on Rockets

Akshaj Arora*, Sahitya Singh, Irina Gordion, and Shawn Carpenter

Ansys Inc., Canonsburg, PA 15317, USA

ABSTRACT: We present a full-physics simulation workflow for modelling the installation and isolation of flush-mounted antenna arrays on rockets, which employs a combination of finite array domain decomposition method (FADDM) and shooting and bouncing rays (SBR) solver. An advanced domain decomposition method is first demonstrated, incorporating 'non-identical' unit cells to efficiently solve a 4×4 antenna array residing in a metal cavity and operating in the X-band at 8.5 GHz. The proposed workflow eliminates the need for any computer-aided design (CAD) modifications for constructing conformal geometries of antennas and recesses in the fuselage, enabling seamless flush mounting of the array into an accurate model of a SpaceX Dragon capsule. The SBR simulation in the workflow is enabled with essential methodologies such as automatic current conformance, creeping-wave physics, physical theory of diffraction, uniform theory of diffraction and current source reduction technique to obtain a high-fidelity yet computationally economical solution that determines radiation characteristics of installed antenna array and isolation between two flush-mounted antenna arrays.

1. INTRODUCTION

Space vehicles and rockets often contain multiple antennas for communications, navigation, remote sensing, data relay, etc. [1–4]. It is well known that crucial antenna characteristics like radiation pattern and input impedance of the installed antennas are impacted by the surface of the fuselage [5–7]. Furthermore, poor antenna placement can result in inadequate isolation between on-board antennas, which causes electromagnetic interference (EMI) between the co-sited radio frequency (RF) systems placed in proximity [8, 9]. Measurement of the antennas installed on rockets is an expensive, time-consuming, and inconvenient process, as most of these electrically large platforms require enormous antenna measurement chambers. Additionally, measurements can only be carried out after the antenna system is fully installed on the platform, which limits the analysis of antenna performance at different locations on the same platform. Therefore, precisely modelling the installation and isolation of antennas on rockets and other space vehicles is imperative to the success of a mission, and remains an ongoing area of research [10].

In recent years, there has been growing interest in flush-mounted antennas for aerospace applications [11–17], as they are seamlessly integrated into the skin of the planar and curved platforms, providing low-profile, less air drag, and more resilience to potential corrosion and deformations due to high-speed mobility as compared to their protruding counterparts. Flush-mounted antennas do not protrude from the fuselage because they are usually placed in a cavity created in the vehicle structure such that their radomes align with the outer skin of the fuselage. Modelling of the flush-mounted antenna arrays on realistic electrically large platforms and accounting for mutual coupling among multiple of such arrays is a challenging problem. Firstly, significant computer-aided design (CAD) manipulations are required to create recesses in the fuselage and conformal geometries of the antennas, and the complexity further increases with the number of installed antennas. Secondly, most space communications are conducted between 300 MHz and 40 GHz [18], and using full-wave methods like Finite Element Method (FEM), Method-of-Moment (MoM) solvers is challenging and computationally demanding due to the enormous aspect ratio [19].

One approach to address the challenges associated with the modelling of antennas on platforms is to utilize domain-decomposition solvers [20, 21], which decompose multi-scale problems into subdomains. However, in order to achieve substantial reduction in the computational resource consumption without sacrificing the accuracy of solution, employing a combination of full-wave and ray-tracing techniques is proven to be an effective approach. Many hybrid frameworks like the method of moments-physical optics (MoM-PO) [22, 23], adaptive integral method-physical optics (AIM-PO) [24], uniform geometrical theory of diffraction-antenna current Green's function (UTD-ACGF) [25], alternating-direction implicit finite-difference time-domain (ADI-FDTD) [26], MoM-SBR [27], and others have been developed to analyze antenna arrays embedded in complex platforms. However, none of these hybrid methods incorporate a realistic simulation of antenna arrays within a cavity which includes accounting for the effects of boundary elements, radome, and metal cavity on antenna characteristics. Moreover, they lack automatic flush-mounting capability, necessitating extensive CAD manipulations to integrate the arrays within the platform. Furthermore, these

* Corresponding author: Akshaj Arora (aarora@gradcenter.cuny.edu).

methods utilize only a limited subset of ray-tracing techniques, which can potentially lead to decreased accuracy.

In this work, we present a high-fidelity hybrid FADDM-SBR hierarchical simulation workflow in the Ansys high frequency structure simulator (HFSS) [28] for analyzing the installation and isolation of antennas on rockets. Historically, antenna arrays are efficiently solved with the finite array domain decomposition method (FADDM), which allows for modelling of finite arrays with only a single identical unit cell [29]. In the proposed simulation workflow, we first demonstrate an advanced FADDM technique for solving a 4×4 patch antenna array residing in a metal cavity (Figure 1), which can only be constructed by using distinct unit cells. This advanced FADDM overcomes the limitation of traditional FADDM by modelling the antenna arrays with multiple 'non-identical' unit cells, while significantly expediting simulations and concurrently reducing memory overhead in comparison with arrays solved with full-wave FEM.

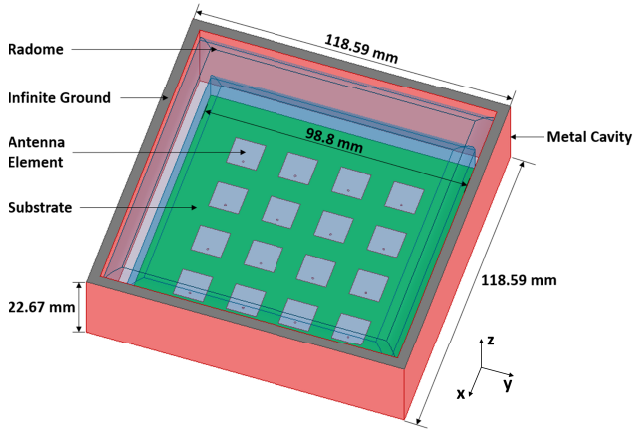

FIGURE 1. Explicit antenna array.

The designed array is modelled with a unique assignment of the perfectly conducting (PEC) infinite ground plane, which bypasses the need to cut a hole in the fuselage, allowing for automatic flush-mounting of the antenna array such that it does not protrude from the fuselage. This method also eliminates the need to explicitly craft conformal geometries for the antennas. The near fields obtained from the advanced FADDM are converted into current sources in the SBR simulation to evaluate the installed antenna performance and determine the isolation between two such installed antenna arrays on a rocket. SBR is an asymptotic ray-tracing method; it is a hybridization of physical optics (PO) and geometric optics (GO), where the PO technique is extended to multi-bounce geometries by using GO ray-tracing [30]. SBR method in HFSS is referred to as HFSS SBR+ [28] because it is enabled with the uniform geometrical theory of diffraction (UTD), physical theory of diffraction (PTD), and creeping wave physics to account for the diffraction of fields at high frequencies and beyond the shadow boundary on the platforms [31–34]. The accuracy of the HFSS SBR+ solver has been validated by both analytical results [35, 36] and measurements [37, 38], and its usage has been demonstrated for various applications like radar signature of realistic objects [39, 40], antennas installed on platforms [32, 41], and advanced driver assistance systems (ADASs) [36, 42, 43]. The proposed simulation workflow can be further extended to model the installation and isolation of antenna arrays on other electrically large platforms like ships, airplanes, and satellites.

This paper is organized as follows. Section 2 discusses the hybrid-hierarchical simulation workflow, detailing the design and analysis of an antenna array residing in a metal cavity, and its installation on an accurate model of a SpaceX Dragon capsule [44]. The isolation between two antenna arrays embedded in the Dragon platform is discussed in Section 3. Finally, the proposed hybrid simulation approach is extended to installed conformal antennas, and is benchmarked against full-wave FEM simulation in Section 4. All the simulations in this paper are performed in off-the-shelf HFSS by leveraging multiple solvers within the software [28].

2. HYBRID SIMULATION WORKFLOW

2.1. Design and Analysis of the Antenna Array in a Metal Cavity

In this study, the 3D component array workflow in HFSS [28] is leveraged to analyze the antenna array shown in Figure 1. This is an efficient, iterative domain-decomposition-based FEM technique for modeling finite periodic structures with non-identical unit cells; it is an extension of the traditional FADDM, which was originally used only for solving arrays with single unit cells [29]. To demonstrate this workflow, we consider a coaxial-fed 4×4 rectangular patch antenna array (Figure 1) operating at 8.5 GHz, which is covered by a dielectric radome made of teflon ($\epsilon_r = 2.1$), and the array along with the radome resides in a perfect electric metal cavity. The HFSS 3D

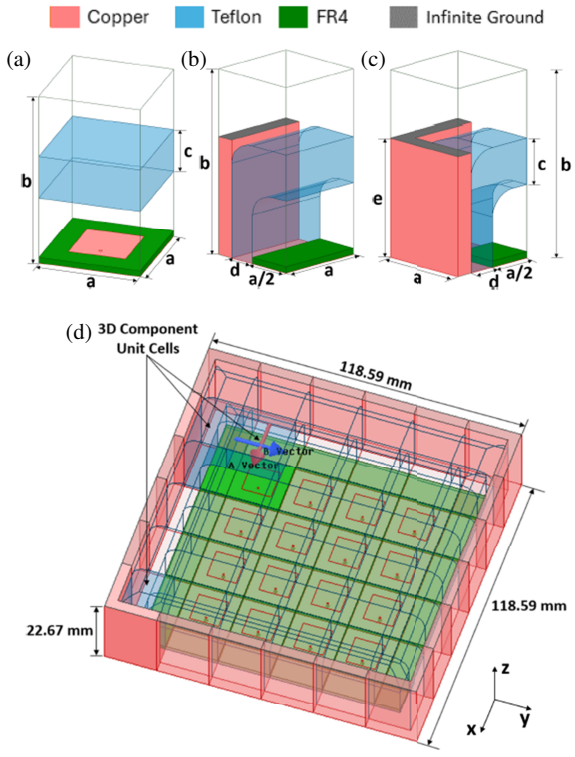

FIGURE 2. (a) Antenna unit cell. (b) Side unit cell. (c) Corner unit cell. (d) 3D component antenna array.

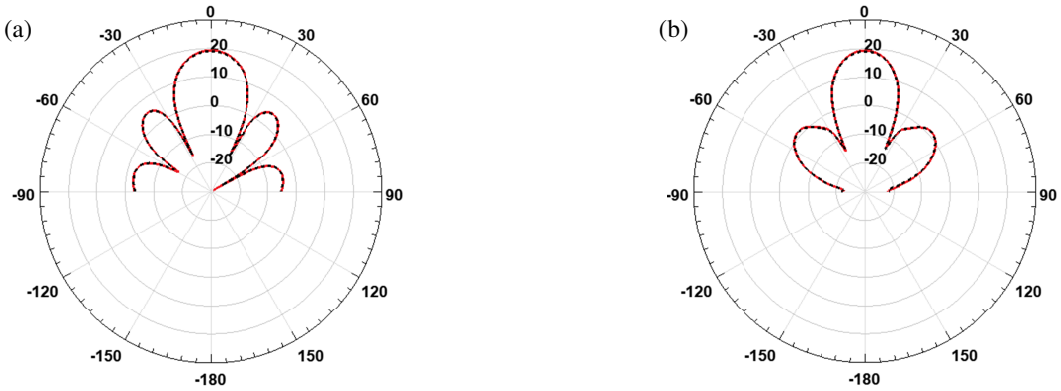

FIGURE 3. Radiation patterns of explicit (solid red line) and 3D component array (short dash black line). (a) xz-plane. (b) yz-plane.

TABLE 1. Dimensions of the unit cells.

variables	length (in mm)
a	19.76
b	50.11
c	12.16
d	6.09
e	32.48

component array method exploits the principle that the antenna array in Figure 1 can be constructed with three distinct unit cells (Figures 2(a), 2(b), and 2(c)), whose dimensions are mentioned in Table 1. After solving these three unit cells separately, the solver copies the converged mesh to each respective element of the 3D component array (Figure 2(d)). The domain decomposition method is employed to divide the array into non-identical sub-domains that are solved in parallel; it is followed by an iterative process to stitch solutions between the sub-domains, which leads to faster simulation time and memory usage reduction [45]. As shown in Figure 3, the far-field radiation patterns of explicit (solved with full-wave FEM) and 3D component arrays agree nearly perfectly in the region above the horizon. The antenna array displays a directive radiation pattern and the peak realized gains obtained from FEM and advanced FADDM techniques are 18.92 dB and 18.89 dB, respectively.

For antennas placed inside metal cavities, electromagnetic fields can either exist within the cavity or protrude out from the top. The fields that contribute to the far-field or near-field patterns, cross-talk between the arrays on the platform, and other relevant interactions are those that protrude from the cavity. Since the array is designed to be embedded into the skin of the SpaceX Dragon capsule model shown in Figure 4, a perfect electric boundary condition with infinite ground (grey in Figure 1) is assigned to the top surface of the metal cavity. This unconventional boundary assignment allows for accurate capturing of electric (E-) and magnetic (H-) fields that protrude from the cavity as the top-ground plane extends to infinity. It precludes any truncated ground plane effects, suppressing all the backward radiation in the FEM or FADDM simulation (Figure 3). The finite and unusual top-ground surface effects originating from the platform are introduced when the installed array is analyzed in the SBR simulation (Figure 6). This special boundary assignment along with the near-field link between the full-wave and ray-tracing simulations bypasses the need to cut a hole in the fuselage and allows for automatic flush-mounting of the antenna array.

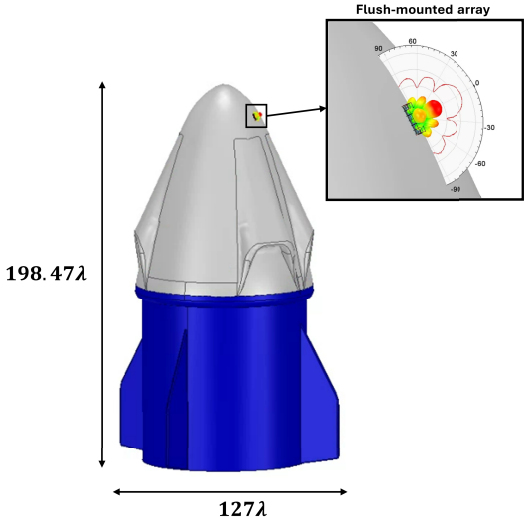

FIGURE 4. 4×4 3D component antenna array installed on the SpaceX Dragon capsule.

All simulations are conducted on a 16-core workstation enabled with 256 GB RAM, and the simulation criterion of $\Delta S < 0.02$ is considered for solving the arrays, where ΔS is the difference in magnitude of the element input port S-parameters between the two adaptive passes in the solve process. The solve times and memory usage for both explicit arrays and 3D component arrays (solved with the advanced FADDM) of different sizes are given in Table 2. The HFSS 3D component array workflow applied to the 4×4 array reduces the simulation run time from 4.68 min to 1.88 min and the memory usage from 6.23 GB to 5.06 GB, with a negligible difference of 0.03 dB in the peak realized gain. For 16×16 array, it reduces the simulation run time from 328.66 min to 41.13 min and the memory usage from 211 GB to 94.1 GB. It is evident that the 3D component array workflow achieves greater speedup and reduced memory requirements as the array size increases, making it an optimal solution for solving large arrays.

TABLE 2. Performance comparison between the Explicit Arrays (full-FEM) and 3D Component Arrays (advanced FADDM) in HFSS.

Array Size	Explicit Array		3D Component Array	
	Run Time	Memory	Run Time	Memory
4×4	4.68 min	6.23 GB	1.88 min (2.48x faster)	5.06 GB
8×8	26.51 min	26.2 GB	5.28 min (5x faster)	23.6 GB
16×16	328.66 min	211 GB	41.13 min (8x faster)	94.1 GB

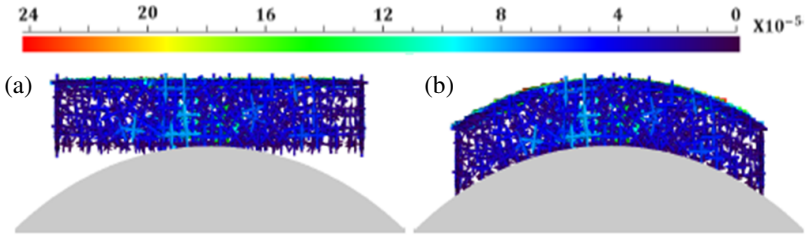

FIGURE 5. Current moments generated by the 3D component antenna array in the HFSS SBR+ simulation. (a) Non-conformal current sources. (b) Conformal current sources.

2.2. Installed Performance Modeling of Antenna Array Mounted on Rocket

The antenna characteristics in free-space change when the same antenna is installed on a platform. This discrepancy is mainly due to the non-ideal ground plane effects, multi-path effects due to reflections in metal structures, creeping waves on curved metal surfaces, and diffraction due to the metal surfaces. HFSS SBR+ solver was leveraged to evaluate the performance of the installed antenna array shown in Figure 2(d), and it utilizes geometrical optics (GO) to launch many rays weighted by the current distribution of the transmitting antenna, which 'paint' physical optics (PO) currents on the surface of the platform. A coherent sum of the radiation contributions from the distributed currents is then directed towards the observation point to obtain the radiation pattern of the antenna integrated in the platform.

In this section, the installed antenna performance of the proposed 3D component antenna array is evaluated. The array is embedded into the skin of SpaceX Dragon capsule, such that the top surface of the metal cavity aligns with the outer surface of the rocket. An accurate model of a Dragon capsule ($198.47\lambda \times 127\lambda \times 127\lambda$ at 8.5 GHz) shown in Figure 4 is considered in this study, and it is assigned as perfect electric conductor (PEC). The array is excited with a composite excitation, where all the 16 ports are active, and a coherent sum of their magnitudes and phases is used as a single source. The weighted combination of a certain excitation pattern allows for only a single beam configuration, which is broadside in this case. The integration of array on the platform is achieved by using a near-field link [28], which is based on the application of the Love's equivalence principal to the fields at the finite element boundary integral (FE-BI) surfaces of the FADDM array [46, 47]: the E- and H-fields extracted from the FADDM simulations are sampled and then converted to equivalent surface current moments, which become the basis for the electric and magnetic current sources in the SBR method. In the event of a change in the placement position of the installed antenna, a re-run of FADDM simulation is not required, and only the HFSS SBR+ simulation needs to be conducted.

The near-field current source model from the advanced FADDM simulation is obtained with a single solution for a flat array. As the antenna is embedded into the skin of the rocket, instead of creating a curved top surface of the metal cavity to align with the curvature of the platform, the automatic current conformance feature [28] of the solver is leveraged to ensure that the current sources above the top surface of the cavity conform to the surface of the rocket. The solver performs conforming of current sources by moving each individual current source a short distance to match the displacement between the original flat plane of the array and the actual installed location surface. Therefore, current sources at the edges of the array surface will be moved a longer distance than those at the center for a typical phased array integrated into a curved surface. The original array plane coincides with the installed vehicle surface at the designated attachment point, so current sources at this location will experience no translation. Figure 5 shows the non-conformal and conformal currents generated by the 3D component array in the SBR simulation.

In order to accurately characterize the back radiation of the installed array, it is necessary to take the creeping-wave effects into account. Creeping waves (CWs) extend the currents induced by the top-ground plane of the antenna array across the curved host platform, which are crucial for determining the back lobe and deep side lobes shadowed by the platform. Figure 6 illustrates the two principal cuts of the far-field radiation pattern of the installed 3D component array obtained from SBR-only solution and SBR solution enabled with CWs, UTD rays, and PTD corrections. The SBR-only solution underestimates the back-lobe gain by 6.83 dB, which can be detrimental to the array performance.

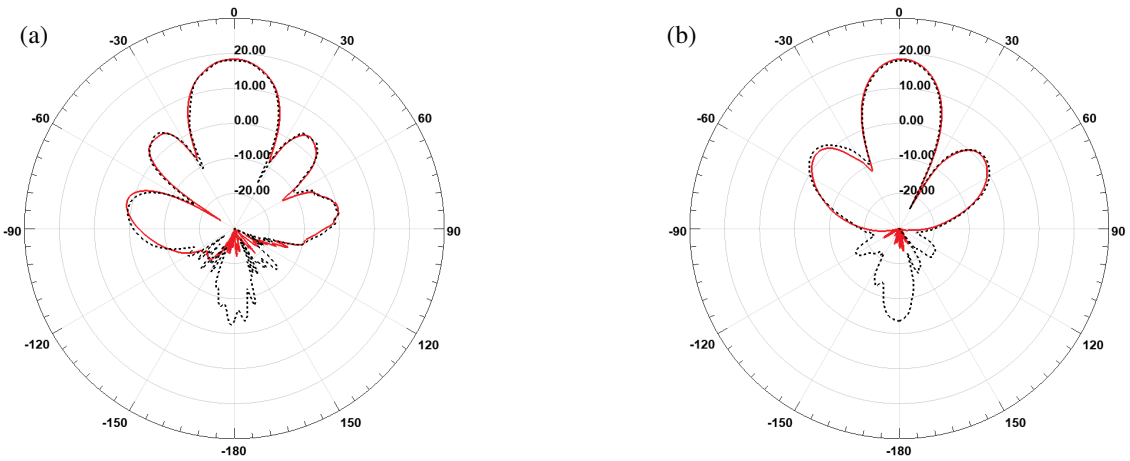

FIGURE 6. Radiation patterns of the installed array obtained from the SBR-only solve without CWs, UTD rays and PTD corrections (solid red line) and SBR solve enabled with the CWs, UTD rays and PTD corrections (short dash black line). (a) xz-plane. (b) yz-plane.

3. ISOLATION BETWEEN ANTENNA ARRAYS INSTALLED ON ROCKET

In this section, isolation between the two antenna arrays buried in the SpaceX Dragon capsule model (Figure 7) is discussed. The arrays make an angle of 60° at the apex of the conical curve such that there is no direct line of sight (LoS) between them. Both the transmitting (Tx) and receiving (Rx) arrays are operating at 8.5 GHz, and are installed using the methodology discussed in Section 2.

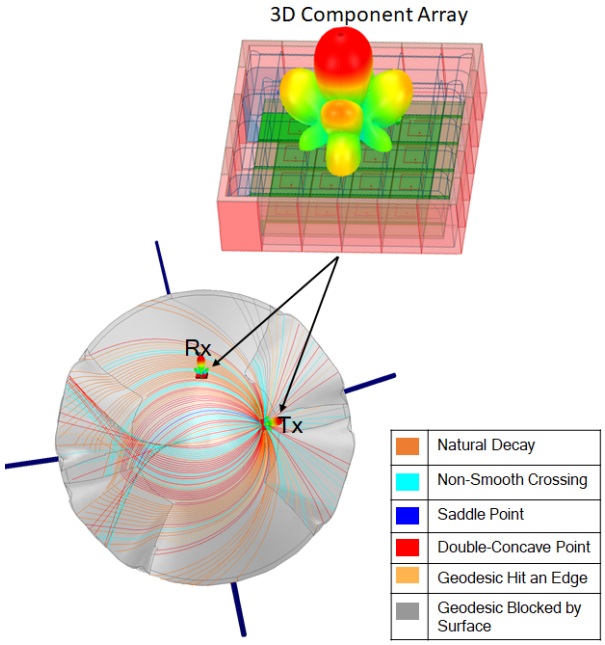

FIGURE 7. Virtual ray tracing of creeping waves launched by the Tx array.

As discussed in Section 2.2, creeping waves play a critical role in estimating the fields past the shadow region, so they are employed in this study to accurately determine the isolation between Tx and Rx arrays. Creeping waves travel along geodesic paths on a convex curved surface and are terminated if they hit a hard discontinuity such as an edge in the model geometry. While further propagating along the surface, painted currents get weaker and creeping waves keep shedding energy. These replacement currents radiate strongly and contribute to the overall scattered field [31]. Figure 7 represents the virtual ray tracing of the deployed CWs generated from Tx array, which are color-coded based on the different termination types.

SBR solve process enabled with the creeping wave physics, PTD corrections and UTD corrections requires considerable computational resources to determine the isolation between arrays because each array is characterized by thousands of current sources. When antennas are represented by current sources (CSRCs), simulation time grows in proportion to the number of CSRCs, and for antenna-to-antenna coupling simulations, this effect is multiplicative, not additive. Nevertheless, many of these sources are weak, and their contribution to the mutual coupling can be neglected. The current source (CSRC) thinning technique can be employed to eliminate the weak CSRCs according to their relative power [28]. For instance, 99% CSRC thinning means that the solver will only retain the current sources associated with the highest 99% of the total power in the array. However, it is important to carefully determine the criterion for the source thinning because the strongest CSRCs serve to reinforce the main beam, and the removal of low-power current sources impacts the accuracy of sidelobe prediction. Since CSRCs can both reinforce and cancel mutual radiation, their elimination may also change the direction of sidelobes. Underestimation and rotation of the sidelobes, especially at the array's horizon, affects the radiation energy that couples with the surface and creeping waves, which can yield inaccurate coupling values.

Figure 8(a) demonstrates the isolation (S_{21}) between the antenna arrays installed on the Dragon capsule for both cases of no CSRC thinning and 99% CSRC thinning. Since there is no direct LoS between the arrays, the mutual coupling is weak and is obtained only by the virtue of creeping waves. The coupling between the arrays with and without applying CSRC thinning is -80.78 dB and -80.25 dB, respectively at 8.5 GHz. For a single frequency point, the antenna coupling simulation with full current sources is solved in 11 hours and 12 minutes, whereas

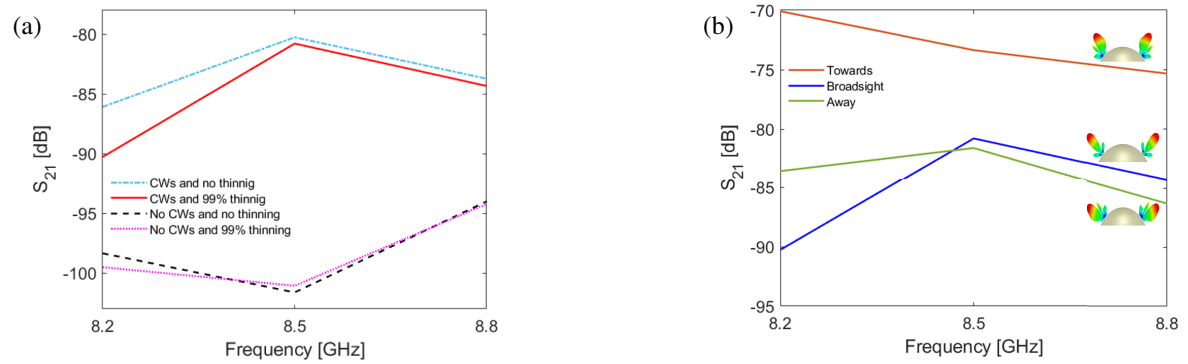

FIGURE 8. (a) Impact of the creeping waves and current source thinning on the isolation between the Tx and Rx arrays. (b) Isolation between the Tx and Rx arrays for different beam configurations.

the simulation with 99% CSRC thinning is solved in 6 hours and 9 minutes. This 45% acceleration in the simulation run time is a consequence of implementing CSRC thinning, which eliminated 36.7% of the weak current sources. The run time drops substantially further — to 2.65 minutes — when the creeping wave physics, PTD and UTD corrections are not considered, but in this case cross-coupling is underestimated by more than 20 dB, which can be detrimental for RF-Cosite interference analysis. All the antenna-to-antenna coupling simulations were solved on a 30-core machine enabled with 182 GB RAM and NVIDIA GRID T4-8Q GPU.

The proposed hybrid simulation workflow with enabled CSRC thinning technique, CWs, and PTD and UTD corrections significantly reduces the simulation time with minimal loss in the fidelity. The amount of acceleration achieved by CSRC thinning and accuracy loss depends on the power distribution of the current sources, which is not only different for every antenna source, but also varies for different beam configurations. Figure 8(b) presents the isolation between the installed arrays obtained from the hybrid simulation enabled with CWs and 99% CSRC thinning for three beam configurations: broadside, and when the main lobe of both arrays is steered to the maximum extent toward and away from each other. It is apparent that even with no direct LoS, the highest co-site coupling occurs when each array is steered to its maximum extent towards the other array.

4. FIDELITY OF THE PROPOSED WORKFLOW AND ITS APPLICATION TO INSTALLED CONFORMAL ANTENNAS

In this section, we apply the proposed hybrid simulation approach to the conformal antennas and benchmark it against FEM in HFSS. Due to high computational expense, it is impractical to utilize full-wave FEM for evaluating the installed antenna performance and isolation between two arrays on the SpaceX Dragon capsule. Therefore, a realizable problem of two identical 4×8 series-fed rectangular patch arrays wrapped on a PEC cylinder (Figure 9) is considered. In order to be consistent with the problem discussed in Sections 2 and 3, the installed conformal arrays have no direct line of sight (LoS), and they make an angle ϕ with the center of axis of the cylinder. The arrays are designed to operate in the X-band at 9.06 GHz, and the dimensions of each patch antenna element are 13.19 mm$\times$10.08 mm.

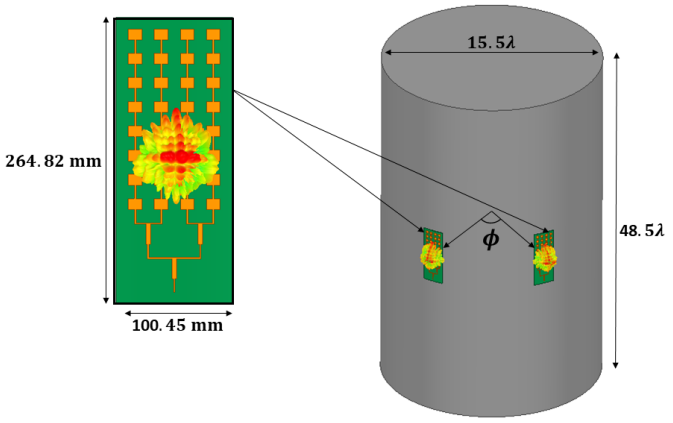

FIGURE 9. Two conformal 4×8 series-fed rectangular patch arrays installed on a PEC cylinder.

This problem is solved using the same methodology as discussed in Sections 2 and 3. Firstly, HFSS 3D component array workflow is used to analyze the 4×8 rectangular patch array. A perfect electric boundary condition with infinite ground plane is assigned to the ground plane of the array, allowing for the inclusion of finite ground plane effects when the array is installed on the PEC cylinder in the HFSS SBR+ simulation. The near-field link captures the E- and H-fields from the 3D component array (advanced FADDM) simulation and converts them to current sources for the SBR method. The current conformance feature in the HFSS SBR+ solver automatically wraps the current sources around the PEC cylinder (Figure 9), without requiring any computer-aided design (CAD) manipulations. Ultimately, the radiation pattern and isolation between the two installed conformal arrays is evaluated by utilizing the SBR method, which is enabled with creeping wave physics, UTD rays, and PTD corrections. On the other hand, the full-wave FEM simulation is configured with an initial step involving CAD modifications to explicitly wrap the 4×8 rectangular patch array onto the PEC cylinder. Subsequently, following the installation of two such arrays, the FEM method is used to determine radiation pattern and isolation between installed conformal arrays.

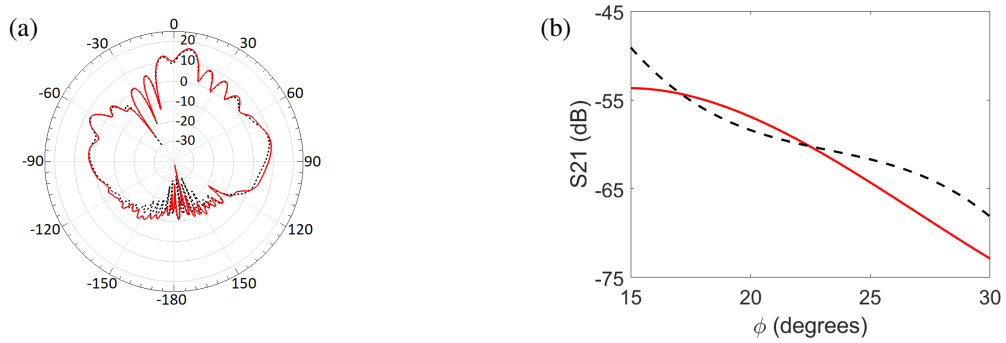

FIGURE 10. Comparison between full FEM (solid red line) and the proposed hybrid (short dash black line) simulation of the two arrays installed on a PEC cylinder. (a) Radiation pattern along the vertical axis of the array. (b) Isolation between the arrays.

Figure 10(a) shows an excellent agreement between the far-field radiation pattern along the vertical axis of a single installed array obtained from the proposed hybrid solution and full-wave FEM simulation, and the peak realized gains obtained from the two simulations are 16.35 dB and 16.83 dB, respectively. As illustrated in Figure 10(b), the increase in the angular distance between the arrays results in a higher level of isolation between them. It is noteworthy that comparable isolation levels are obtained from both simulation techniques employed. For a single angular distance, the solver performance for this geometry is summarized in Table 3. As expected, the FEM simulation is more computationally demanding because the PEC cylinder is electrically large. The purposed hybrid solution reduces the total simulation run time from 471.8 min to 25.2 min and the memory usage from 31.4 GB to 3.04 GB. For the hybrid solution, it required 12.93 min and 3 GB to solve the array with advanced FADDM solver and 12.26 min and 40.8 MB to solve for the installation and isolation of antennas on the PEC cylinder by utilizing SBR simulation enabled with CWs, UTD, and PTD. As mentioned in Section 2.2, in the event of change in the installed position of the antenna arrays, a rerun of FADDM simulation is not required, and only the SBR simulation enabled with CWs, UTD, and PTD is conducted, which allows to significantly reduce computational resources and simulation run time.

TABLE 3. Performance comparison between the Finite Element Method (FEM) and hybrid solution.

Simulation Type	Run Time	Memory
FEM	471 min 48 s	31.4 GB
Hybrid Solution	25 min 12 s	3.04 GB

5. CONCLUSION

Unfavorable antenna placement and poor isolation between the flush-mounted antennas is detrimental to the co-sited RF systems. In most cases, measurements are expensive, time-consuming, and can only accommodate limited analysis. Numerical analysis of the installed antennas is also a challenging problem because of large electrical sizes of the rockets at GHz frequencies and enormous aspect ratios. Therefore, including the proposed hybrid hierarchical simulation approach enabled with creeping wave physics, current source thinning technique, and HFSS 3D component array workflow in the pre-design cycle is an effective approach for investigating installed array performance and isolation between the antenna arrays on rockets. The hybrid simulation approach allows for modelling of realistic antenna arrays with 'non-identical' unit cells; it significantly reduces the simulation time and computational resources required for such large-scale simulations with minimal loss in accuracy, and it bypasses the need for any CAD manipulation to create recesses in the fuselage or explicitly wrapping antennas on curved objects. The proposed workflow can be extended to model installation and isolation of a diverse class of cavity-backed and conformal antenna arrays on realistic electrically large platforms like ships, cars, aircrafts, and others.

ACKNOWLEDGEMENT

The authors would like to thank Sara Louie and Tadahiro Negishi for their valuable suggestions and contributions during the development of this work.

REFERENCES

[1] Monk, A., P. Martens, Y. Inasawa, N. Yoneda, I. Naito, M. Miyazaki, Y. Shimawaki, Y. Konishi, A. Iida, and S. Makino, "Ultra-low profile airborne reflector antenna subsystem for broadband satellite communications," in *21st International Communications Satellite Systems Conference and Exhibit*, 2316, 2003.

[2] Eom, S. Y., S. H. Son, Y. B. Jung, S. I. Jeon, S. A. Ganin, A. G. Shubov, A. K. Tobolev, and A. V. Shishlov, "Design and test of a mobile antenna system with tri-band operation for broadband satellite communications and DBS reception," *IEEE Transactions on Antennas and Propagation*, Vol. 55, No. 11, 3123–3133, 2007.

[3] Jung, Y.-B., S.-Y. Eom, S.-I. Jeon, A. V. Shishlov, and C.-J. Kim, "Novel hybrid antenna design having a shaped reflector for mobile satellite communication applications," in *2010 IEEE Antennas and Propagation Society International Symposium*, 1–4, Toronto, ON, Canada, Jul. 2010.

[4] Akan, V. and E. Yazgan, "Antennas for space applications," *Advanced Radio Frequency Antennas for Modern Communication and Medical Systems*, 139, 2020.

[5] Gao, S.-P., B. Wang, H. Zhao, W.-J. Zhao, and C. E. Png, "Installed radiation pattern of patch antennas: Prediction based on a novel equivalent model," *IEEE Antennas and Propagation Magazine*, Vol. 57, No. 3, 81–94, 2015.

[6] Burkholder, R. J., K. Sertel, P. H. Pathak, J. L. Volakis, and S. S. Navale, "Analysis of radiation and coupling associated with large multiple antenna arrays on ships," in *IEEE Antennas and Propagation Society Symposium, 2004*, Vol. 3, 2687–2690, Monterey, CA, USA, Jun. 2004.

[7] Chatterjee, D., C. J. Reddy, and R. J. Burkholder, "Conformal arrays on variable curvature surfaces: An assessment of mutual coupling analysis," in *2013 IEEE International Symposium on Phased Array Systems and Technology*, 821–824, Waltham, MA, USA, Oct. 2013.

[8] Koper, E. M., W. D. Wood, and S. W. Schneider, "Aircraft antenna coupling minimization using genetic algorithms and approximations," *IEEE Transactions on Aerospace and Electronic Systems*, Vol. 40, No. 2, 742–751, 2004.

[9] Kolodziej, K. E. and B. T. Perry, "Vehicle-mounted STAR antenna isolation performance," in *2015 IEEE International Symposium on Antennas and Propagation & USNC/URSI National Radio Science Meeting*, 1602–1603, Vancouver, BC, Canada, Jul. 2015.

[10] Pazos, J. J., M. C. Miller, J. Phillips, E. Miller, T. McDonald, and J. Kitaygorsky, "Estimating fields in spacecraft cavities: Experimental validation and optimization of finite-difference time-domain and power balance computational tools," *IEEE Journal on Multiscale and Multiphysics Computational Techniques*, Vol. 7, 276–284, 2022.

[11] Rufail, L. and J.-J. Laurin, "Aircraft cavity-backed nonprotruding wideband antenna," *IEEE Antennas and Wireless Propagation Letters*, Vol. 11, 1108–1111, 2012.

[12] Elmansouri, M. A. and D. S. Filipovic, "Ultrawideband flush-mounted antenna," *IEEE Antennas and Wireless Propagation Letters*, Vol. 16, 1973–1976, 2017.

[13] Nguyen-Trong, N., S. P. Pinapati, D. Hall, A. Piotrowski, and C. Fumeaux, "Ultralow-profile and flush-mounted monopolar antennas integrated into a metallic cavity," *IEEE Antennas and Wireless Propagation Letters*, Vol. 17, No. 1, 86–89, 2017.

[14] Chen, Z. and Z. Shen, "Wideband flush-mounted surface wave antenna of very low profile," *IEEE Transactions on Antennas and Propagation*, Vol. 63, No. 6, 2430–2438, 2015.

[15] Tianang, E. G., M. A. Elmansouri, and D. S. Filipovic, "Ultra-wideband lossless cavity-backed vivaldi antenna," *IEEE Transactions on Antennas and Propagation*, Vol. 66, No. 1, 115–124, 2017.

[16] Che, J.-K., C.-C. Chen, and J. F. Locke, "A compact cavity-backed tri-band antenna design for flush mount GNSS (L1/L5) and SDARS operations," *IEEE Antennas and Wireless Propagation Letters*, Vol. 20, No. 5, 638–642, 2021.

[17] Ding, X., Y.-F. Cheng, X.-S. Yang, B.-Z. Wang, and D. E. Anagnostou, "A flush-mounted quasi-full-space beam-scanning cylindrical phased array," *IEEE Transactions on Antennas and Propagation*, Vol. 67, No. 7, 4883–4888, 2019.

[18] NASA, "NASA communications." Available: https://www.nasa.gov/smallsat-institute/sst-soa/soa-communications/, 2024.

[19] Chew, W. C., E. Michielssen, J. M. Song, and J.-M. Jin, *Fast and Efficient Algorithms in Computational Electromagnetics*, Artech House, Inc., 2001.

[20] Gao, H.-W., S. Wang, X.-Q. Sheng, and Z. Peng, "Rapid numerical analysis of electrically large PEC platforms with local variations via a platform Green's Function method," *IEEE Transactions on Antennas and Propagation*, Vol. 70, No. 10, 9544–9556, 2022.

[21] Solis, D. M., V. F. Martin, M. G. Araújo, D. Larios, F. Obelleiro, and J. M. Taboada, "Accurate emc engineering on realistic platforms using an integral equation domain decomposition approach," *IEEE Transactions on Antennas and Propagation*, Vol. 68, No. 4, 3002–3015, 2019.

[22] Liu, Z.-L., X. Wang, and C.-F. Wang, "Installed performance modeling of complex antenna array mounted on extremely large-scale platform using fast MoM-PO hybrid framework," *IEEE Transactions on Antennas and Propagation*, Vol. 62, No. 7, 3852–3858, 2014.

[23] Deng, J.-Y. and L.-X. Guo, "An efficient octree-based Mom-PO method for analysis of antennas on large platform," *IEEE Antennas and Wireless Propagation Letters*, Vol. 14, 819–822, 2015.

[24] Wang, X., S.-X. Gong, J. Ma, and C.-F. Wang, "Efficient analysis of antennas mounted on large-scale complex platforms using hybrid AIM-PO technique," *IEEE Transactions on Antennas and Propagation*, Vol. 62, No. 3, 1517–1523, 2014.

[25] Kim, Y.-D., H.-J. Kim, K.-U. Bae, J.-H. Park, and N.-H. Myung, "A hybrid UTD-ACGF technique for DOA finding of receiving antenna array on complex environment," *IEEE Transactions on Antennas and Propagation*, Vol. 63, No. 11, 5045–5055, 2015.

[26] Liang, Z.-X., H. Xie, Y. Guo, J. Wang, E.-P. Li, Z. Zhao, H. Zhou, H. Chen, and W.-Y. Yin, "Improved hybrid leapfrog ADI-FDTD method for simulating near-field coupling effects among multiple thin wire monopole antennas on a complex platform," *IEEE Transactions on Electromagnetic Compatibility*, Vol. 59, No. 2, 618–626, 2016.

[27] Fan, T.-Q., L.-X. Guo, and W. Liu, "A novel OpenGL-based MoM/SBR hybrid method for radiation pattern analysis of an antenna above an electrically large complicated platform," *IEEE Transactions on Antennas and Propagation*, Vol. 64, No. 1, 201–209, 2015.

[28] Ansys, Inc., "HFSS 2025 R1 online help," Canonsburg, PA, USA, 2025.

[29] Commens, M. and K. Zhao, "Finite antenna array analysis with a unit-cell domain decomposition method," in *2012 42nd European Microwave Conference*, 313–316, Amsterdam, Netherlands, Oct.–Nov. 2012.

[30] Ling, H., R.-C. Chou, and S.-W. Lee, "Shooting and bouncing rays: Calculating the RCS of an arbitrarily shaped cavity," *IEEE Transactions on Antennas and Propagation*, Vol. 37, No. 2, 194–205, 1989.

[31] Kipp, R. A., S. M. Canta, T. A. Courtney, and D. L. Setterdahl, "Extending shooting-and-bouncing rays method with creeping waves for radar signature prediction," in *2015 IEEE Radar Conference (RadarCon)*, 0704–0707, Arlington, VA, USA, May 2015.

[32] Kipp, R. A. and I. Capoglu, "Extending shooting-and-bouncing rays method with uniform theory of diffraction for installed antennas," in *2014 IEEE Antennas and Propagation Society International Symposium (APSURSI)*, 2198–2199, Memphis, TN, USA, Sep. 2014.

[33] Mologni, J. F., J. C. Ribas, M. A. R. Alves, and C. S. Arismar, "Deployment of a fast and accurate hybrid FEM/M0M/FEBI/SBR+ methodology for ship EMC design," in *2017 IEEE 3rd Global Electromagnetic Compatibility Conference (GEMCCON)*, 1–4, Sao Paulo, Brazil, Nov. 2017.

[34] Zhao, K. and L. E. R. Petersson, "Overview of hybrid solver in HFSS," in *2018 IEEE International Symposium on Antennas and Propagation & USNC/URSI National Radio Science Meeting*, 411–412, Boston, MA, USA, Jul. 2018.

[35] Chipengo, U., "Full physics simulation of terrain-adaptive 77 GHz automotive radar for early pedestrian detection," *Microwave and Optical Technology Letters*, Vol. 61, No. 5, 1375–1380, 2019.

[36] Castro, J. D., S. Singh, A. Arora, S. Louie, and D. Senic, "Enabling safe autonomous vehicles by advanced mm-wave radar simulations," in *2019 IEEE MTT-S International Microwave Symposium (IMS)*, 1476–1479, Boston, MA, USA, Jun. 2019.

[37] Chipengo, U., A. P. Sligar, S. M. Canta, M. Goldgruber, H. Leibovich, and S. Carpenter, "High fidelity physics simulation-based convolutional neural network for automotive radar target classification using micro-doppler," *IEEE Access*, Vol. 9, 82 597–82 617, 2021.

[38] Chipengo, U., "Validation of electromagnetics simulations for vehicle-to everything applications using measured results," BENCHMARK: The International Magazine for Engineering Designers Analysts from NAFEMS, 22–26, Jan. 2021.

[39] Canta, S. M., R. A. Kipp, S. Carpenter, and L. E. R. Petersson, "Range-Doppler radar signature prediction of wind turbine using SBR," in *12th European Conference on Antennas and Propagation (EuCAP 2018)*, 814, London, UK, Apr. 2018.

[40] Setterdahl, D. L., R. A. Kipp, and M. C. Miller, "Signa: A radar signature prediction tool for electrically large targets," in *2014 IEEE Radar Conference*, 0083–0087, Cincinnati, OH, USA, May 2014.

[41] Chipengo, U., P. M. Krenz, and S. Carpenter, "From antenna design to high fidelity, full physics automotive radar sensor corner case simulation," *Modelling and Simulation in Engineering*, Vol. 2018, No. 1, 4239725, 2018.

[42] Chipengo, U., "Full physics simulation study of guardrail radar-returns for 77 GHz automotive radar systems," *IEEE Access*, Vol. 6, 70 053–70 060, 2018.

[43] Sligar, A. P., "Machine learning-based radar perception for autonomous vehicles using full physics simulation," *IEEE Access*, Vol. 8, 51470–51476, 2020.

[44] SpaceX, "Spacex dragon," Available: https://www.spacex.com/vehicles/dragon/, 2024.

[45] Zhao, K., "A domain decomposition method for solving electrically large electromagnetic problems," Ph.D. dissertation, The Ohio State University, Columbus, Ohio, USA, 2007.

[46] Love, A. E. H., "I. The integration of the equations of propagation of electric waves," *Philosophical Transactions of the Royal Society of London. Series A, Containing Papers of a Mathematical or Physical Character*, Vol. 197, No. 287-299, 1–45, 1901.

[47] Rogier, H., "Advanced applications of the field equivalence principle in numerical electromagnetic modelling techniques," *URSI Radio Science Bulletin*, Vol. 2003, No. 305, 22–29, 2003.